Readout of quantum devices with a sideband microwave interferometer immune to systematic noise

N. Crescini◍,[†] E.G. Kelly◍, G. Salis◍,[*] and A. Fuhrer◍

IBM Research Europe - Zurich, Säumerstrasse 4, 8803 Rüschlikon, Switzerland

The accuracy of microwave measurements is not only critical for applications in telecommunication and radar but also for future quantum computers. Qubit technologies such as superconducting qubits or spin qubits require the detection of minuscule signals, typically achieved by reflecting a microwave tone off a resonator that is coupled to the qubit. Noise from cabling and amplification, e.g., from temperature variations, can be detrimental to readout fidelity. We present an approach to detect phase and amplitude changes of a device under test based on the differential measurement of microwave tones generated by two first-order sidebands of a carrier signal. The two microwave tones are sent through the same cable to the measured device that exhibits a narrow-band response for one sideband and leaves the other unaffected. The reflected sidebands are interfered by down-conversion with the carrier. By choosing the amplitude and phases of the sidebands, suppression of either common-amplitude or common-phase noise can be achieved, allowing for fast, stable measurements of frequency shifts and quality factors of resonators. Test measurements were performed on NbN superconducting resonators at 25 mK to calibrate and characterize the experimental setup and to study time-dependent fluctuations of their resonance frequency.

I. INTRODUCTION

Interferometric measurements are among the most sensitive and well studied in experimental physics. Their application ranges from fundamental physics and metrology to quantum information [1–4] and they are of transversal interest for many other fields of research [5,6]. In an optical interferometer, the probe and reference laser beams follow distinct paths and their interference is indicative of relative variations between the two paths [see Fig. 1(a)]. Microwave interferometers can also be realized in this way [7] and have been used to measure frequency variations of devices such as resonators [8–14]. For qubit readout in solid state quantum processors [4,15–22] or to measure frequency variations and noise in resonators used for kinetic inductance detectors [23–25], standard single-sideband (SSB) detection is employed to convert a variation of the microwave signal to base band. In that scheme, a modulation signal is up- and down-converted in frequency

allowing for sensitive measurements at high frequency with relatively inexpensive base-band instrumentation.

One of the advantages of interferometric measurements is their insensitivity to common-mode noise or long-term drifts common to both interfering paths. Measurements where the two paths are likely to experience differential noise—e.g., when a microwave signal senses a sample in a cryostat and is then referenced to a carrier signal routed outside the cryostat—cannot benefit from this suppression and the signal will be affected by variations in temperature, losses of microwave components or amplification noise specific to one path.

Here, we demonstrate how the two paths of an interferometer in the microwave domain can be substituted by two different frequencies, thus using a bichromatic signal along the same physical path (e.g., the same cable going into and out of a cryostat). In this case, a relative phase or amplitude shift between the two microwave tones produces the desired signal, whereas noise in amplitude or phase common to the two tones can be suppressed.

The basic idea to separate the two interfering signals in the frequency domain is shown in Fig. 1(b). Our approach is based on sideband modulation of a carrier signal and is thus referred to as a sideband microwave interferometer (SMI). We describe the implementation and characterization of the SMI, provide a theoretical model, and experimentally verify the suppression of common-mode phase noise and amplitude noise at two different operation points
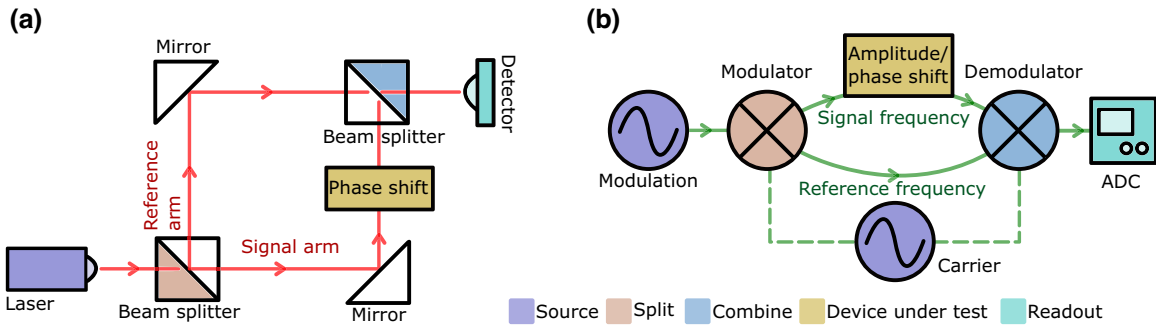

FIG. 1.   A comparison between (a) an optical Mach-Zehnder interferometer and (b) a microwave sideband interferometer such as the one presented in this work. In (a), a laser is split into two rays that follow different paths and eventually interfere on a detector. In (b), the signal follows the same path but contains two sidebands of different frequency, where only one is affected by the device under test (DUT). Down-conversion with the carrier signal yields the interference signal whose phase and amplitude is measured by analog-to-digital conversion (ADC).

of the interferometer. The setup is then used to probe the response of a coplanar-waveguide resonator at millikelvin temperatures, allowing rapid microwave measurements of fluctuations of the frequency and quality factor of the resonator induced by two-level systems (TLSs). The experiment is implemented with a signal generator, a splitter, two mixers, and a lock-in amplifier. The bandwidth is limited by the shortest lock-in integration time and in the present case can extend up to tens of megahertz, allowing for the measurement of fast variations, although at the expense of the detection sensitivity.

In Sec. II, we provide a detailed explanation of the measurement scheme and its experimental implementation. Section III shows the operation of the SMI and characterization of its noise-suppression properties. In Sec. IV we conclude and provide perspectives on improvements with which we plan to advance our scheme.

II. MEASUREMENT SCHEME

The general idea [see Fig. 1(b)] is to modulate a microwave carrier signal to generate two sidebands. These are reflected off or transmitted through a device under test (DUT) and then demodulated to make them interfere. In contrast to conventional SSB detection [26], the interference allows for the detection of relative phase or amplitude changes between the two sidebands, which can be exploited to obtain a first-order suppression of the common-mode noise introduced, e.g., in the cable by thermal expansion or vibrations. For instance, one sideband can be tuned to the frequency of a resonator and be used as a probe, while the other one may lie several line widths away, acting as a reference. The parameters of the SMI can be tuned to obtain an output signal that is proportional to a constructive or destructive interference of the two reflected or transmitted sidebands, thus reducing either common-mode phase or amplitude noise.

The definitions of the various frequencies used in this work are reported in Table I in Appendix A and are

hereafter used to detail the theoretical description of this method.

Figure 2 shows the setup used in this work. The carrier signal proportional to $e^{i\omega_0 t}$ is modulated in an in-phase and quadrature (IQ) mixer with I and Q signals $a_1 e^{i\omega_s t + i\alpha_1}$ and $a_2 e^{i\omega_s t + i\alpha_2}$ generated by a lock-in amplifier. This creates two first-order sidebands at frequencies $\omega_{1,2} = \omega_0 \pm \omega_s$. The amplitudes and phases of the two sidebands can be selected by setting the modulation parameters a_1, a_2, α_1, and α_2. More specifically, the sidebands are proportional to $a_1 e^{i\omega_1 t + i\alpha_1} - a_2 e^{i\omega_1 t + i\alpha_2}$ and $a_1 e^{i\omega_2 t - i\alpha_1} + a_2 e^{i\omega_2 t - i\alpha_2}$.

In our case, the signal is then attenuated in multiple steps (by a total of 90 dB) and sent to a coplanar-waveguide resonator in a dilution refrigerator. The reflected signal is amplified by a low-noise cryogenic amplifier (LNA) at 4 K. A second amplification stage at room temperature further increases the signal strength, resulting in a combined amplification of 70 dB. The output signal is then down-converted by mixing it with the carrier signal $e^{i\omega_0 t + i\theta}$ at a second mixer (accounting for a phase difference θ of the carrier signal between the two mixers). The output of
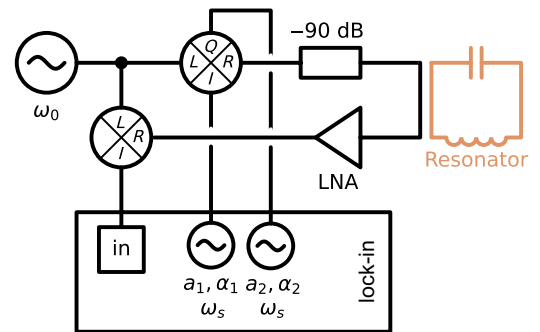

FIG. 2.   The schematics of the experimental setup. Here, -90 dB indicates the estimated attenuation of the microwave lines in the cryostat, while LNA denotes the low-noise-amplification chain both at cryogenic and at room temperature.
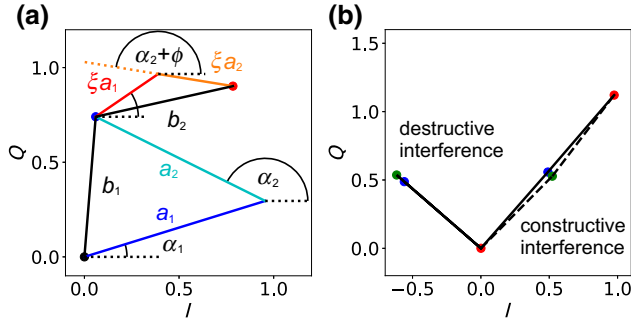
FIG. 3. The interference of the down-converted signal in the complex plane. (a) Four terms in Eq. (1) of the up- and down-converted signal after acquiring a phase shift ϕ and an attenuation ξ at the lower sideband frequency, where the red dot indicates the resulting interference of the two terms b_1 and b_2. Note that we assume that $\theta = 0.0$ rad. (b) Two situations with parameters adjusted to obtain constructive interference, where the common phase-noise is suppressed, or destructive interference, where the common amplitude-noise is suppressed. The blue dots correspond to positions of b_1 without common-mode offsets and the green dots are obtained by either adding a phase offset of 0.06 rad to both sidebands (for constructive interference, $\theta = -0.64$ rad) or by increasing the amplitude of both sidebands by 10% (for destructive interference, $\theta = 0.94$ rad). The parameter values used are as follows: $a_1 = a_2 = 1.0$, $\alpha_1 = 0.3$ rad, $\alpha_2 = 2.68$ rad, $\xi = 0.4$, and $\phi = 0.3$ rad.

the latter is finally measured using the lock-in amplifier, yielding IQ components x and y.

For simplicity, we assume that the DUT only affects the signal at frequency ω_1; in this sense, the two sidebands can be referred to as probe (ω_1) and reference (ω_2). We assume that the DUT shifts the phase of the probe sideband by ϕ and reduces its amplitude by a factor ξ. Neglecting the terms that oscillate with $2\omega_0$, the output signal of the SMI that is measured by the lock-in amplifier is

$$s_{\text{out}}(t) = a_1 e^{i\omega_s t + i\alpha_1 + i\theta} + \xi a_1 e^{i\omega_s t + i\alpha_1 + i\phi - i\theta}$$
$$+ a_2 e^{i\omega_s t + i\alpha_2 + i\theta} - \xi a_2 e^{i\omega_s t + i\alpha_2 + i\phi - i\theta}. \quad (1)$$

The IQ components of the terms oscillating at ω_s in Eq. (1) are visualized in Fig. 3(a). The total signal can be understood as two interfering terms, $b_1 e^{i\beta_1} = a_1 e^{i\alpha_1 + i\theta} + a_2 e^{i\alpha_2 + i\theta}$ and $b_2 e^{i\beta_2} = \xi e^{i\phi}(a_1 e^{i\alpha_1 - i\theta} - a_2 e^{i\alpha_2 - i\theta})$. The amplitudes b_1 and b_2 are given by

$$b_1^2 = a_1^2 + a_2^2 + 2a_1 a_2 \cos(\alpha_1 - \alpha_2) \quad (2)$$

and

$$b_2^2 = \xi^2 \left(a_1^2 + a_2^2 - 2a_1 a_2 \cos(\alpha_1 - \alpha_2)\right). \quad (3)$$

By tuning the parameters of the modulation signals (a_1, α_1, a_2, α_2, and θ), we can achieve identical amplitudes for the two interfering terms, $b_1 = b_2$, and an arbitrary phase

$\beta_1 - \beta_2$ between them. The parameters for same amplitudes are found by equating Eq. (2) with Eq. (3), yielding the condition $\cos(\alpha_1 - \alpha_2) = (\xi^2 - 1)(a_1^2 + a_2^2)/((1 + \xi^2)(2a_1 a_2))$. The phase $\beta_1 - \beta_2$ can be tuned by adapting a_1, a_2, and either $\alpha_1 - \alpha_2$ or θ.

There are two phases of specific interest, geometrically illustrated in Fig. 3(b): for $\beta_1 - \beta_2 = 0$, we achieve constructive interference and common-mode phase noise at the two sideband frequencies is suppressed. For $\beta_1 - \beta_2 = \pi$, we achieve destructive interference, where common noise in the amplitude of the two sidebands is canceled. For both destructive and constructive interference, the signal demodulated by the lock-in amplifier senses ξ and ϕ, in a similar way as in conventional SSB detection schemes but here with the added advantage of suppressed common-mode noise.

III. TEST AND CALIBRATION OF THE SIDEBAND INTERFEROMETER

A. Phase- and amplitude-noise rejection

To verify the predicted common-mode amplitude-noise and phase-noise rejection, we use the interferometric scheme reported in Fig. 2 but replace the resonator with a variable attenuator and a variable phase shifter. We determine the optimal rejection points for both noise sources by applying either a controlled attenuation or a controlled phase shift to the up-converted signal. In Fig. 4, we compare the magnitude of the noise sensitivity $\Delta S = \sqrt{\Delta x^2 + \Delta y^2}$ as a function of varying a_2 and α_2 (at a fixed a_1 of 10 mV and α_1 of 5.76 rad). Δx and Δy correspond to the changes of the I and Q components x and y of the demodulated signal when varying the common-mode amplitude by 1 % or the common-mode phase by 0.01 rad. Note that 0.01 rad corresponds to a typical phase shift of a 5 GHz signal in a 5-m-long coaxial cable when the temperature drifts by 1 K. The detailed experimental setup is presented in Appendix A.

Common amplitude-noise is suppressed at $x = y = 0.0$ mV [see Fig. 4(a)] as predicted in Sec. II and because of destructive interference of the two sidebands. We reach this point at $a_2 = 43.7$ mV and $\alpha_2 = 4.30$ rad. The line cut of ΔS versus x at $y = 0.0$ mV in Fig. 4(c) shows that ΔS decreases linearly toward the rejection point. Similarly, the common-mode phase noise [see Fig. 4(b)] is linearly suppressed toward its rejection point at $x = 1.7$ mV and $y = 0.0$ mV [see Fig. 4(d)]. This point corresponds to $a_2 = 23.2$ mV and $\alpha_2 = 1.00$ rad. The values in Figs. 4(c) and 4(d) can be compared to the noise sensitivity at the SSB configuration [$a_2 = 11$ mV and $\alpha_2 = 1.06$ rad; crosses in Figs. 4(a) and 4(b)], where ΔS is 7.6 µV for both 1 % of amplitude noise or 0.01 rad of common-mode phase change. These results demonstrate experimentally that the SMI can to first order suppress either form of common-mode noise by adjusting the amplitude and phase of the
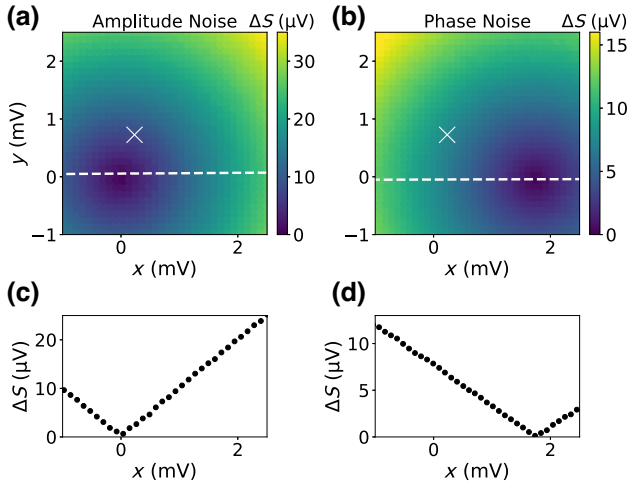
FIG. 4. The measured signal variation ΔS for a common modulation of (a) the amplitudes of the two sidebands by 1 % and (b) the phase of the two sidebands by 0.01 rad. These quantities are shown at different working points in the IQ plane of the SMI obtained by varying a_2 and α_2, for fixed a_1 and α_1. The white cross indicates the single-sideband point in the IQ plane. (c),(d) At the optimal working points, the influence of either noise source linearly approaches zero, as seen in the cross sections, which are taken at the dashed white lines in (a) and (b).

two lock-in outputs. We expect that the ultimate limit of such suppression is given by the stability of phases and amplitudes of the lock-in outputs and by that of the carrier signals used for the up- and down-conversion.

B. Resonator measurements

The interference between the two sidebands distorts the signal in the IQ plane as compared to the SSB case. To demonstrate that the SMI can nevertheless be used to obtain quantitative values of the complex signal amplitude, we test it on a high kinetic inductance coplanar-waveguide resonator in a hanger geometry, fabricated from a thin film of sputtered NbN with a nominal thickness of 10 nm on an intrinsic silicon substrate. The resonator has a length of 2 mm. Its resonance frequency is $f_r = 6.16$ GHz, the loaded and coupling quality factors are $Q_l \simeq 8.0 \times 10^3$ and $Q_c \simeq 9.8 \times 10^3$, and the resonator has an impedance $Z_r \simeq 316$ Ω. Since the low-power internal quality factor is of order $Q_i \simeq 5 \times 10^4$, the resonator is overcoupled. Measurements are performed at 25 mK, the base temperature of a dilution refrigerator. For more details, the reader is referred to the appendixes, which show the measured probe signal (microwave output) of the SMI and the phase and amplitude response of the resonator under study.

If the frequency of the probe sideband is set to the center frequency of the resonator, $\omega_r/2\pi$, a small variation of ω_r by $\delta_r \ll \gamma_r$ mostly affects the phase ϕ of the reflected sideband. Here, γ_r is the resonator line width. With the SMI probing at a fixed frequency, only frequency shifts $\delta_r < \gamma_r$
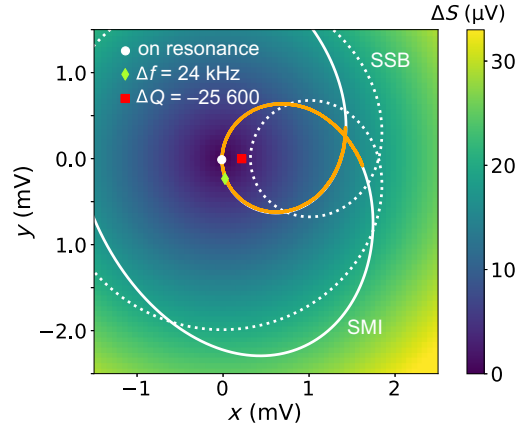

FIG. 5. The spectroscopy of a resonator and comparison of SSB and SMI signal in the IQ plane. The dashed curve shows the calculated reflection from the resonator in the IQ plane for normal single-sideband detection and makes the link to the VNA data shown in Fig. 7 in Appendix A. The orange line is the measured data in amplitude-noise rejection configuration of the SMI. The solid line is the fitted theoretical curve of the interferometric readout. For noise measurements, the probe frequency was set close to the resonance frequency of the resonator (white dot). Small variations in resonator frequency (green diamond, frequency shift of 24 kHz) or resonator quality factor (red dot, reduction of internal quality factor from Q_i to $Q_i/2$) correspond to orthogonal directions in the IQ plane. The color scale indicates the magnitude ΔS of changes of the signal in the IQ plane when assuming 1 % of common-mode amplitude noise on both sidebands.

can be resolved. For larger $\delta_r \gg \gamma_r$, the signal exceeds the measurement bandwidth (MBW) and changes in ϕ or ξ become very small.

To determine absolute frequency shifts of the resonator, it is necessary to relate the SMI signal to the resonance line shape. The latter is obtained from SSB spectroscopy by sweeping the frequency of the carrier ω_0 in an interval $\simeq \gamma_r$, with ω_1 close to the resonator frequency, and independently with a vector network analyzer (VNA). In Fig. 5, this is shown together with the signal, where the SMI is tuned to the amplitude-noise-suppression point at $\omega_1 = \omega_r$ (orange curve). Note that the electrical phase delay (i.e., a background phase component linearly varying with frequency) leads to a circular (elliptical) background signal in the SSB (SMI) configuration, respectively. If probed on resonance, small shifts of the resonator frequency affect mostly the phase ϕ of the reflected probe sideband, whereas variations in the quality factor change the reflected amplitude ξ, changing the SMI signal in the orthogonal direction in the IQ plane of the demodulated signal. In Fig. 5, we indicate the calculated SMI signal for a resonator with reduced internal quality factor (red square) and with a shifted resonance frequency (green diamond).
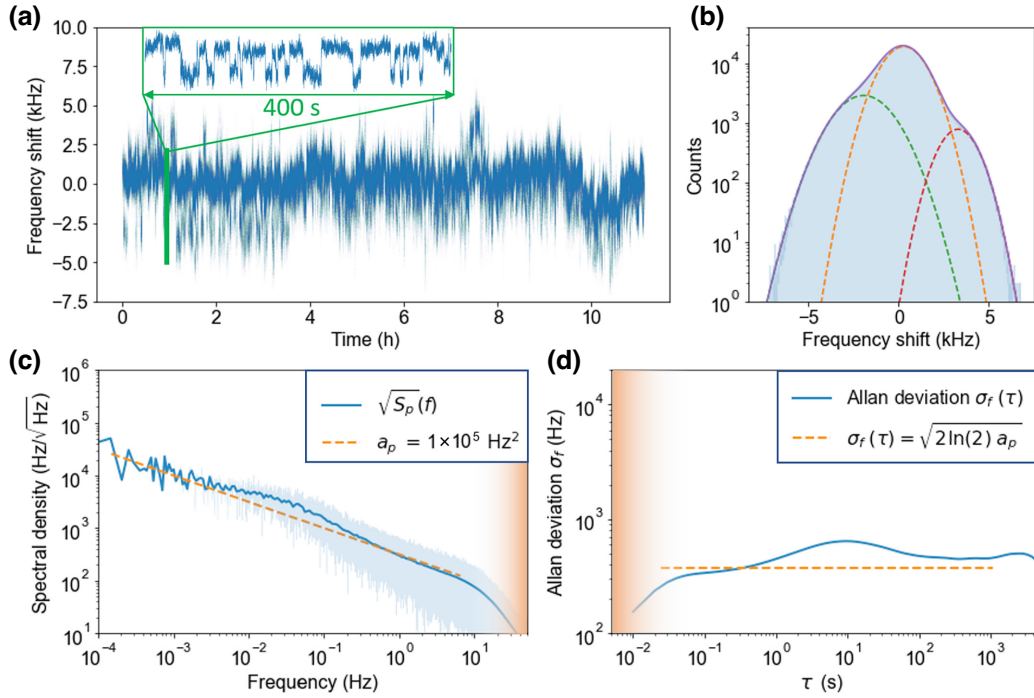
FIG. 6.   The SMI measurement of the frequency fluctuations of a test resonator: (a) a time trace, (b) a histogram, (c) the spectral density $\sqrt{S_p}$, and (d) the Allan deviation $\sigma_f(\tau)$ of the same data set. The average photon number in this measurement is $\langle n \rangle \simeq 8$. The dashed brown lines indicate the expected a_p/f behavior of the power spectrum S_p and the brown shading indicates the limit imposed by the measurement bandwidth.

C. Study of resonator noise

Noise in microwave resonators usually originates from the presence of TLSs in amorphous materials or interfaces of these devices [27–30]. Due to the relevance for improving coherence of quantum devices, this is the object of an intense research activity [31–40]. Techniques that track frequency fluctuations [41] can shed light on the properties of TLSs [14,42,43] and have brought about new possibilities for studying their distribution, origin, and stability [43–50]. In this context, the SMI, which allows suppression of common-mode noise, can be a powerful tool to gain further insights into the underlying TLS physics.

We have measured the resonator frequency fluctuations for more than 11 h at a time and an example trace is reported in Fig. 6(a). Even though the signal has been recorded with the SMI tuned to the amplitude-noise rejection point to also capture fluctuations in the Q factor (not shown), the sensitivity to common-mode phase noise remains below a factor of 2 compared to the SSB configuration (see Appendix C). The frequency fluctuations of the resonator were obtained from the SMI signal using a calibration as discussed in Sec. III B and using a linear interpolation between SMI phase and resonator frequency. The detected noise increases by more than a factor of 100 with respect to the signal measured off resonance and is thus dominated by the fluctuations of the resonator. The

average photon occupation number was calculated using [38]

$$\langle n \rangle = \frac{E_r}{\hbar \omega_r} = \frac{2}{\hbar \omega_r^2} \frac{Q_l^2}{Q_c} \frac{50\Omega}{Z_r} P_{\text{in}}, \tag{4}$$

where P_{in} is the input power of the on-resonance sideband. In this measurement, the resonator is studied with $\langle n \rangle \simeq 8$. The sampling frequency is set to 100 Hz and the lock-in integration time is 10 ms.

The time trace of the resonator frequency, shown in Fig. 6(a), displays clear random telegraph signals (see the inset) typically associated with TLS noise. The histogram [Fig. 6(b)], spectral density [Fig. 6(c)], and Allen deviation [Fig. 6(d)] put a slightly different spotlight on the TLS properties. The histogram [Fig. 6(b)] of the time trace in Fig. 6(a) can be fitted with three shifted Gaussians. This seems to indicate that a few slow TLSs dominate the disturbance of the resonator and lead to three large characteristic frequency shifts. In an ensemble of TLSs, a few near-resonant fluctuators can be more strongly coupled to the resonator [28], giving rise to such discrete offsets. The noise spectrum $\sqrt{S_p}$ in Fig. 6(c) is obtained through a Fourier transform of the time trace after subtracting offsets and by application of a moving average in the frequency domain. Here, we expect to see an ensemble of

TLSs show up as the typical $S_p = a_p/f$ dependence (the dashed line). There are two obvious deviations from this behavior in the data. Above 10 Hz, we see that the noise is suppressed due to the measurement bandwidth limited by the lock-in integration time (the brown shading). At around 20 mHz, we find more noise than expected from the $1/f$ background. We argue that this is due to a characteristic time scale of the dominant TLSs that contribute to an additional broad peak in the spectrum [43]. A comparison with the inset in Fig. 6(a) shows that the switching frequency of the dominant TLS is compatible with this value. Another, complementary, way of visualizing this is the Allan deviation $\sigma_f(\tau)$, shown in Fig. 6(d). The Allan deviation is typically used to estimate the frequency stability of oscillators and is obtained by averaging increasingly long fractions of a time trace. For a a_p/f power spectrum, it should be constant at a level of $\sigma_f(\tau) = \sqrt{2 \ln 2 a_p}$ (the dashed line). We again find a peak centered around $\tau = 1/(2\pi 20 \text{ mHz}) \approx 8$ s and a reduction of the noise at small τ. We have also studied the dependence of these noise spectra and Allan deviations down to photon numbers $\langle n \rangle < 0.1$, where white noise dominates the spectrum for frequencies >0.2 Hz and the low-frequency fluctuation amplitude of the resonator increases to $a_p = 4.0 \cdot 10^6$ Hz^2 (see Appendix D). These findings are in agreement with previously reported results (see, e.g., Refs. [14,43]).

This shows that the application of the SMI to the study of TLS noise is promising. The fact that variations in the frequency and Q value of the resonator lead to orthogonal signals in the SMI readout (see Fig. 5) can be used to simultaneously track both frequency and quality factor shifts of a quantum device [42]. This allows the study of noise correlations in these two values, something that we will explore in a forthcoming work.

IV. CONCLUSIONS AND PERSPECTIVES

We describe and operate a microwave interferometer based on the modulation of a carrier resulting in two sidebands, which are used as probe and reference signals. This setup measures relative phase or amplitude shifts between the probe and the reference, therefore selectively eliminating common-mode noise and enabling long-term stability in quantum device characterization. We test our scheme by adding controlled common-phase and -amplitude variations that demonstrate the resilience of the scheme to systematic noise. The SMI is advantageous over conventional SSB if the routing of the up-converted signal to the DUT and back experiences noise or drift in phase or amplitude that differs from the noise experienced by the carrier used for down-conversion. Examples include cases where the signal needs to be routed over long cables affected by temperature changes or vibrations, which typically occurs if the DUT is placed inside a cryostat. We use the SMI for the readout of a superconducting resonator at millikelvin

temperatures and measure its frequency noise, which is induced by nearby TLS fluctuators.

The ultimate sensitivity that can be reached with this setup is not thoroughly addressed in this work but will be the subject of future analysis. A critically coupled resonator could be read out at lower power with the same signal-to-noise ratio. Exploiting this, one could test the noise of a resonator with a much lower photon number $\langle n \rangle$ or increase the MBW to study higher-frequency noise. Note that the SMI cannot suppress noise that is correlated at the two sideband frequencies, e.g., high-frequency noise introduced by an LNA. In the case of frequency shifts that exceed the line width of the resonator, a feedback loop with a proportional integral differential (PID) controller could be implemented via software in the lock-in amplifier, in order to track the resonance frequency and extend the MBW of the present experiment. This addition does not necessarily reduce the signal bandwidth, as the PID could be integrated digitally in the lock-in.

In the present work, the potential of the SMI is demonstrated in a study of TLS noise affecting a coplanar-waveguide resonator but we stress that its application is far more general. For instance, the properties of the SMI can be leveraged for the readout of qubits at lower power and reduced sensitivity to systematic sources of noise such as slow drifts induced by temperature fluctuations. Instead of using the two sidebands as probe and reference, the principle of sideband interference can be extended by using both sidebands as a probe, e.g., of two different resonators, each coupled to a qubit. This could enable parity readout of the two qubits with reduced common-mode noise.

APPENDIX A: ADDITIONAL EXPERIMENTAL DETAILS

Table I lists names, symbols, short descriptions, and values of important quantities and abbreviations used in the main text.

The spectrum of the microwave signal that is used to probe the resonator is shown in Fig. 7(a), which is also

TABLE I.   The definition of the different frequencies that are relevant for this setup.

Name	Symbol	Description	Indicative value
Carrier frequency	$\omega_0/2\pi$	Frequency of the microwave oscillator	6.16 GHz
Modulation frequency	$\omega_s/2\pi$	Frequency of the phase and quadrature inputs of the IQ mixer	10 MHz
Sideband frequencies	$\omega_{1,2}/2\pi$	Sideband microwave frequencies	$\omega_0 \pm \omega_s$
Resonator frequency	$\omega_r/2\pi$	Average resonator frequency	$\omega_0/2\pi$
Resonator line width	$\gamma_r/2\pi$	Average resonator line width	100 kHz
Resonator shift	$\delta_r/2\pi$	Shift of the resonator frequency	$\sim$10 kHz
Measurement band	MBW	Maximum frequency shift δ_r that the interferometer can detect	$< \gamma_r$
Sampling band	SBW	Maximum frequency of δ_r that can be sampled, corresponding to the minimum lock-in τ of 30 ns	30 MHz
Lock-in bandwidth	LBW	Lock-in amplifier bandwidth, related to the analog-to-digital converter sampling rate of 1.8×10^9 samples/s	600 MHz

helpful to frame the quantities described in the text and in Table I. Figure 7(b) shows the resonator response measured with a VNA. The left sideband is on resonance with ω_r and thus interacts with the resonator, while the right sideband remains unaffected. The signal at the carrier frequency ω_0 is suppressed by roughly 5 orders of magnitude. This is obtained with a carrier power $\simeq 15$ dBm and frequency $\omega_0/2\pi \simeq 6.16$ GHz, while the modulation amplitudes a_1 and a_2 are of order 50 mV and frequencies are $\omega_s/2\pi \simeq 10$ MHz. The IQ mixer is balanced with dc offsets in order to minimize the amplitude of the carrier at the microwave output by more than 4 orders of magnitude. This signal is gradually attenuated by -91 dB and sent to the resonator.

APPENDIX B: EXPERIMENTAL SETUP FOR DEMONSTRATION OF PHASE AND AMPLITUDE-NOISE REJECTION

The experimental setup for the demonstration of phase- and amplitude-noise rejection found in Sec. III A is displayed in Fig. 8. A voltage-controlled variable attenuator and a variable phase shifter were placed in series after the microwave output of the IQ mixer. A dc block was used to prevent any dc leakage from the IQ mixer that would affect the value of either the attenuation or the phase arising from these components. An isolator was placed after each component to prevent the formation of standing waves.

For the common-mode phase-noise measurements, attenuation arising from the phase shifter was calibrated using a single-sideband configuration. A small voltage-dependent attenuation of the phase shifter was
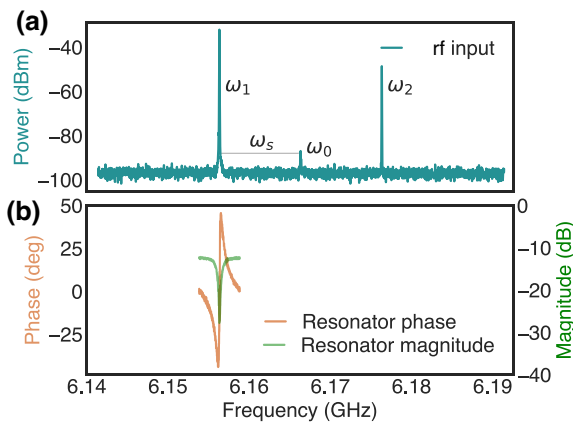

FIG. 7.   The interferometer probe signal and the resonator response. (a) The spectrum of the microwave IQ mixer output signal that is sent to the resonator in the dilution refrigerator, with the probe sideband at ω_1, the reference sideband at ω_2, and a residual carrier signal at ω_0. (b) The phase and magnitude of the resonator line shape that is probed by the sideband at ω_1.
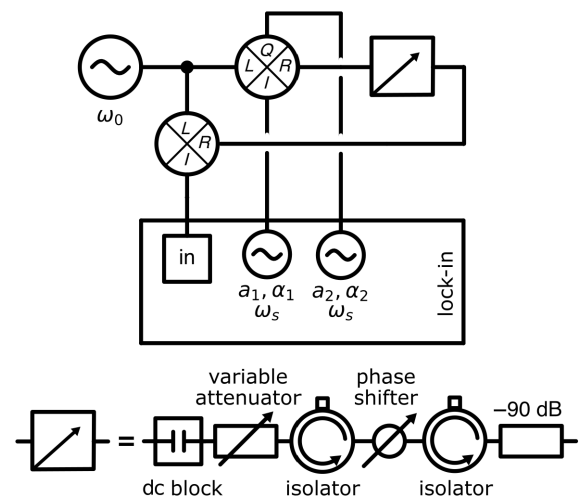

FIG. 8.   A schematic of the experimental setup to demonstrate common-phase and -amplitude rejection.

compensated with the variable attenuator. A common-mode amplitude variation was achieved by varying both amplitudes a_1 and a_2 of the signals coming from the lock-in amplifier.

The different working points in the IQ plane as displayed in Fig. 4 were obtained for different amplitudes a_2 ranging from 0 mV to 80 mV and phases α_2 from 0 to 2π rad of the Q input of the IQ mixer for fixed amplitude $a_1 = 10$ mV and fixed phase α_1.

APPENDIX C: COMMON-MODE NOISE SENSITIVITY ON RESONANCE

While either the common-mode amplitude or phase noise can be suppressed to first order with the SMI, the sensitivity to the respective other type of noise is not enhanced by more than a factor of 2; for the example of the signal of the resonator investigated in this study with the SMI tuned to the amplitude-noise rejection point, see Fig. 9.

APPENDIX D: POWER DEPENDENCE OF RESONATOR NOISE

We have studied the frequency noise of the resonator for different probing powers and, otherwise, the same parameters as in the main text. The resulting noise spectral densities (SD) and Allan deviations are shown in Fig. 10. The measurements reported in the main text are presented in Figs. 10(a) and 10(d), both showing excellent agreement with the expected $1/f$ behavior up to a time scale
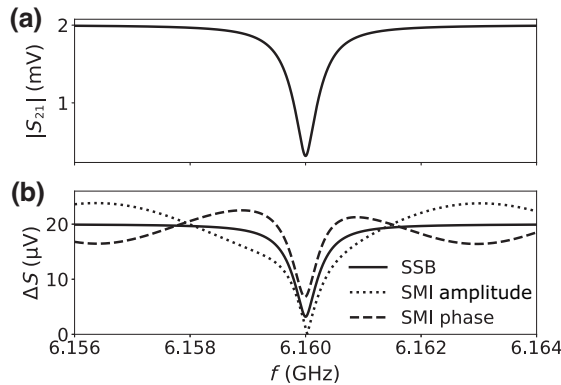

FIG. 9. The noise-sensitivity comparison of the SMI tuned to the amplitude-noise rejection configuration at the resonance frequency of a resonator. (a) The measured amplitude response of the resonator as detected in the SSB configuration. (b) The calculated signal variation ΔS for the SSB configuration (solid line) and for the SMI configuration tuned to the amplitude-noise rejection point, where the dotted line shows ΔS for a common-amplitude change of 1 % and the dashed line for a common-phase change of 10 mrad. In this SMI configuration, amplitude noise is canceled to first order, whereas the effect of phase noise remains low around resonance (about 6.8 µV compared to 3.2 µV in the SSB case).

of several hours. The reduced probing power, used in Figs. 10(b), 10(e), 10(c), and 10(f), decreases the signal-to-noise ratio of the interferometer; therefore measurement noise (white noise) starts to dominate over the noise from the resonator. For both measurements, at weaker probing power the Allan deviation shows a slope closer to -0.5 (green dashed line) at small τ values, which is expected for white noise.

APPENDIX E: GUIDE TO OPERATION

Here, we detail a practical guide to set up an interferometric readout such as the one described in this work. In this context, Fig. 2 is taken as a reference.

(1) A microwave source is taken and its (carrier) frequency ω_0 is tuned close to that of the DUT.

(2) The carrier is then split and the two outputs are connected to the LO ports of an IQ mixer and a down-conversion mixer. In the former, the IQ inputs are wired to two low-frequency oscillators that create sidebands and have the same frequency $\omega_1 = \omega_2$ (but tunable phase α_1 and α_2 and amplitude a_1 and a_2). In our setup, these are the reference outputs of the lock-in amplifier and can therefore also be used for phase-sensitive detection of the down-converted output signal of the SMI. The amplitude of the probe signal can be varied by changing a_1 and a_2 or by attenuating the entire input signal.

(3) At this point, using similar initial values of the two amplitudes and phases, it is convenient to connect the resulting signal to a spectrum analyzer and check the sidebands. The dc offsets of the low-frequency oscillators can eliminate the residual carrier at ω_0 by balancing the mixing and yield a spectrum like the one of Fig. 7(a). This is the input signal that is sent to the DUT, so one should take care that only one sideband is on resonance with the spectral features of the DUT. The output signal of the SMI is down-converted in the second mixer and its phase and amplitude are detected with the lock-in amplifier.

(4) With this, the setup is fully wired and measurements can commence. The first thing to test is that one sideband is actually on resonance with the DUT, which can be done by, e.g., sweeping ω_0 and resolving the spectral features of the DUT on the lock-in output. This spectroscopic measurement can also be fitted to the resonator line shape (measured, e.g., with a VNA) to calibrate the system. Once the resonance of the DUT is found, the amplitude-noise rejection configuration is simply obtained by tweaking a_2 and α_2 to obtain a zero in the amplitude $\sqrt{x^2 + y^2}$ of the output signal, as shown in Fig. 4(a). Before starting measurements, the input signal is checked again and the mixer rebalanced such as to account for intermittent adjustments of the parameters of the oscillator.
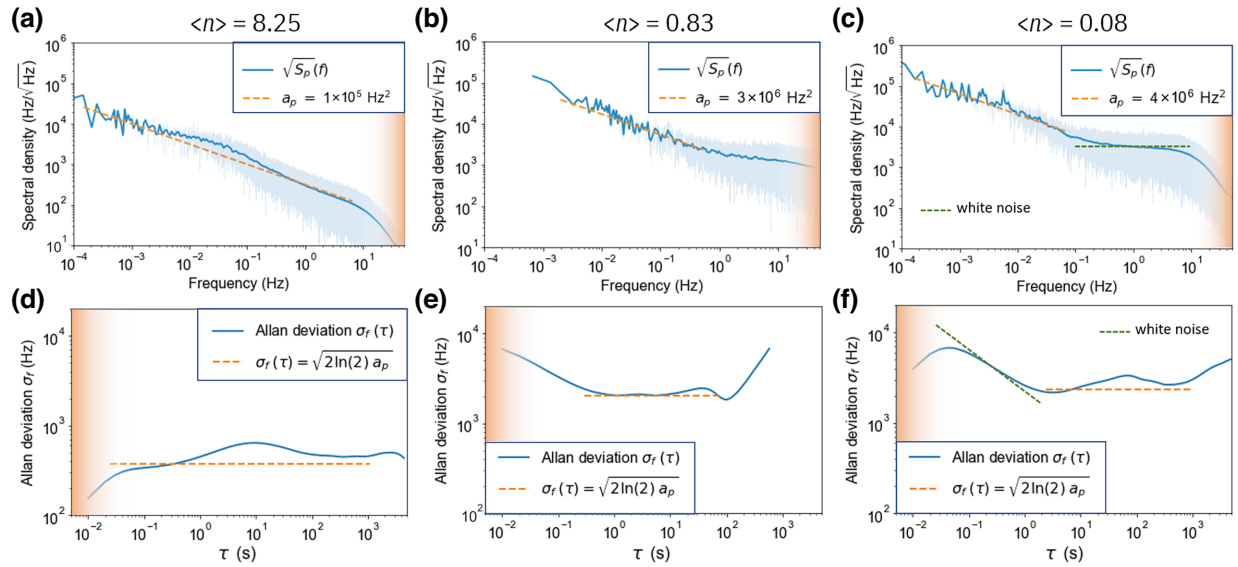
FIG. 10. The measured spectral densities (a)–(c) and Allan deviations (d)–(f) of the system noise for different probing powers, as indicated by the average photon number $\langle n \rangle$ above the plots.

The interferometer is now ready to measure in the amplitude-noise-rejection configuration. The simplest way to switch to phase-noise rejection requires a phase shifter between the splitter and the LO (carrier or local oscillator) input of the down-conversion mixer. The interferometer can be configured to amplitude-noise rejection following the previous procedure and by applying a phase shift of π one ends up in the phase-noise-rejection configuration.

---

[1] P. Fritschel, G. González, B. Lantz, P. Saha, and M. Zucker, High power interferometric phase measurement limited by quantum noise and application to detection of gravitational waves, Phys. Rev. Lett. **80**, 3181 (1998).

[2] F. Hudelist, J. Kong, C. Liu, J. Jing, Z. Y. Ou, and W. Zhang, Quantum metrology with parametric amplifier-based photon correlation interferometers, Nat. Commun. **5**, 3049 (2014).

[3] J. Millerd, N. Brock, J. Hayes, B. Kimbrough, M. Novak, M. North-Morris, and J. C. Wyant, in *Optical Measurement Systems for Industrial Inspection IV*, Vol. 5856, edited by W. Osten, C. Gorecki, and E. L. Novak, International Society for Optics and Photonics (SPIE, 2005), p. 14.

[4] L. S. Martin, W. P. Livingston, S. Hacohen-Gourgy, H. M. Wiseman, and I. Siddiqi, Implementation of a canonical phase measurement with quantum feedback, Nat. Phys. **16**, 1046 (2020).

[5] W. H. Steel, *Interferometry* (Cambridge University Press, Cambridge, 1983).

[6] P. Hariharan, *Optical Interferometry* (Elsevier Science, Amsterdam, 2003), 2nd ed.

[7] D. M. Pozar, *Microwave Engineering* (John Wiley & Sons, New York, 2011), 4th ed.

[8] E. Rubiola, *Phase Noise and Frequency Stability in Oscillators*, The Cambridge RF and Microwave Engineering Series (Cambridge University Press, 2008).

[9] E. Ivanov, M. Tobar, and R. Woode, Microwave interferometry: Application to precision measurements and noise reduction techniques, IEEE Trans. Ultrason. Ferroelectr. Freq. Control **45**, 1526 (1998).

[10] E. Ivanov, M. Tobar, and R. Woode, Applications of interferometric signal processing to phase-noise reduction in microwave oscillators, IEEE Trans. Microw. Theory Tech. **46**, 1537 (1998).

[11] C. A. Regal, J. D. Teufel, and K. W. Lehnert, Measuring nanomechanical motion with a microwave cavity interferometer, Nat. Phys. **4**, 555 (2008).

[12] E. E. Scime, R. F. Boivin, J. L. Kline, and M. M. Balkey, Microwave interferometer for steady-state plasmas, Rev. Sci. Instrum. **72**, 1672 (2001).

[13] O. Tudisco, A. Lucca Fabris, C. Falcetta, L. Accatino, R. De Angelis, M. Manente, F. Ferri, M. Florean, C. Neri, C. Mazzotta, D. Pavarin, F. Pollastrone, G. Rocchi, A. Selmo, L. Tasinato, F. Trezzolani, and A. A. Tuccillo, A microwave interferometer for small and tenuous plasma density measurements, Rev. Sci. Instrum. **84**, 033505 (2013).

[14] T. Lindström, J. Burnett, M. Oxborrow, and A. Y. Tzalenchuk, Pound-locking for characterization of superconducting microresonators, Rev. Sci. Instrum. **82**, 104706 (2011).

[15] A. Crippa, R. Ezzouch, A. Aprá, A. Amisse, R. Laviéville, L. Hutin, B. Bertrand, M. Vinet, M. Urdampilleta, T. Meunier, M. Sanquer, X. Jehl, R. Maurand, and S. De Franceschi, Gate-reflectometry dispersive readout and coherent control of a spin qubit in silicon, Nat. Commun. **10**, 2776 (2019).

[16] E. J. Connors, J. J. Nelson, and J. M. Nichol, Rapid high-fidelity spin-state readout in Si/Si-Ge quantum dots via rf reflectometry, Phys. Rev. Appl. **13**, 024019 (2020).

[17] V. N. Ciriano-Tejel, M. A. Fogarty, S. Schaal, L. Hutin, B. Bertrand, L. Ibberson, M. F. Gonzalez-Zalba, J. Li, Y.-M. Niquet, M. Vinet, and J. J. L. Morton, Spin readout of a CMOS quantum dot by gate reflectometry and spin-dependent tunneling, PRX Quantum **2,** 010353 (2021).

[18] H. Wang, M. Hofheinz, J. Wenner, M. Ansmann, R. C. Bialczak, M. Lenander, E. Lucero, M. Neeley, A. D. O'Connell, D. Sank, M. Weides, A. N. Cleland, and J. M. Martinis, Improving the coherence time of superconducting coplanar resonators, Appl. Phys. Lett. **95,** 233508 (2009).

[19] G. Catelani, R. J. Schoelkopf, M. H. Devoret, and L. I. Glazman, Relaxation and frequency shifts induced by quasiparticles in superconducting qubits, Phys. Rev. B **84,** 064517 (2011).

[20] P. V. Klimov, *et al.*, Fluctuations of energy-relaxation times in superconducting qubits, Phys. Rev. Lett. **121,** 090502 (2018).

[21] S. Schlör, J. Lisenfeld, C. Müller, A. Bilmes, A. Schneider, D. P. Pappas, A. V. Ustinov, and M. Weides, Correlating decoherence in transmon qubits: Low frequency noise by single fluctuators, Phys. Rev. Lett. **123,** 190502 (2019).

[22] J. Lisenfeld, A. Bilmes, S. Matityahu, S. Zanker, M. Marthaler, M. Schechter, G. Schön, A. Shnirman, G. Weiss, and A. V. Ustinov, Decoherence spectroscopy with individual two-level tunneling defects, Sci. Rep. **6,** 23786 (2016).

[23] J. Zmuidzinas, Superconducting microresonators: Physics and applications, Annu. Rev. Condens. Matter Phys. **3,** 169 (2012).

[24] P. K. Day, H. G. LeDuc, B. A. Mazin, A. Vayonakis, and J. Zmuidzinas, A broadband superconducting detector suitable for use in large arrays, Nature **425,** 817 (2003).

[25] J. Baselmans, S. J. C. Yates, R. Barends, Y. J. Y. Lankwarden, J. R. Gao, H. Hoevers, and T. M. Klapwijk, Noise and sensitivity of aluminum kinetic inductance detectors for sub-mm astronomy, J. Low Temp. Phys. **151,** 524 (2008).

[26] B. J. Chapman, E. I. Rosenthal, J. Kerckhoff, L. R. Vale, G. C. Hilton, and K. W. Lehnert, Single-sideband modulator for frequency domain multiplexing of superconducting qubit readout, Appl. Phys. Lett. **110,** 162601 (2017).

[27] L. Faoro and L. B. Ioffe, Internal loss of superconducting resonators induced by interacting two-level systems, Phys. Rev. Lett. **109,** 157005 (2012).

[28] C. Müller, J. H. Cole, and J. Lisenfeld, Towards understanding two-level-systems in amorphous solids: Insights from quantum circuits, Rep. Progr. Phys. **82,** 124501 (2019).

[29] C. Müller, J. Lisenfeld, A. Shnirman, and S. Poletto, Interacting two-level defects as sources of fluctuating high-frequency noise in superconducting circuits, Phys. Rev. B **92,** 035442 (2015).

[30] L. Faoro and L. B. Ioffe, Interacting tunneling model for two-level systems in amorphous materials and its predictions for their dephasing and noise in superconducting microresonators, Phys. Rev. B **91,** 014201 (2015).

[31] J. Gao, J. Zmuidzinas, B. A. Mazin, H. G. LeDuc, and P. K. Day, Noise properties of superconducting coplanar waveguide microwave resonators, Appl. Phys. Lett. **90,** 102507 (2007).

[32] R. Barends, H. L. Hortensius, T. Zijlstra, J. J. A. Baselmans, S. J. C. Yates, J. R. Gao, and T. M. Klapwijk, Contribution of dielectrics to frequency and noise of NbTiN superconducting resonators, Appl. Phys. Lett. **92,** 223502 (2008).

[33] T. Lindström, J. E. Healey, M. S. Colclough, C. M. Muirhead, and A. Y. Tzalenchuk, Properties of superconducting planar resonators at millikelvin temperatures, Phys. Rev. B **80,** 132501 (2009).

[34] R. Barends, H. L. Hortensius, T. Zijlstra, J. J. A. Baselmans, S. J. C. Yates, J. R. Gao, and T. M. Klapwijk, Noise in NbTiN, Al, and Ta superconducting resonators on silicon and sapphire substrates, IEEE Trans. Appl. Supercond. **19,** 936 (2009).

[35] P. Macha, S. H. W. van der Ploeg, G. Oelsner, E. Il'ichev, H.-G. Meyer, S. Wünsch, and M. Siegel, Losses in coplanar waveguide resonators at millikelvin temperatures, Appl. Phys. Lett. **96,** 062503 (2010).

[36] J. Lisenfeld, G. J. Grabovskij, C. Müller, J. H. Cole, G. Weiss, and A. V. Ustinov, Observation of directly interacting coherent two-level systems in an amorphous material, Nat. Commun. **6,** 6182 (2015).

[37] J. Burnett, L. Faoro, and T. Lindström, Analysis of high quality superconducting resonators: Consequences for TLS properties in amorphous oxides, Supercond. Sci. Technol. **29,** 044008 (2016).

[38] A. Bruno, G. de Lange, S. Asaad, K. L. van der Enden, N. K. Langford, and L. DiCarlo, Reducing intrinsic loss in superconducting resonators by surface treatment and deep etching of silicon substrates, Appl. Phys. Lett. **106,** 182601 (2015).

[39] C. Neill, A. Megrant, R. Barends, Y. Chen, B. Chiaro, J. Kelly, J. Y. Mutus, P. J. J. O'Malley, D. Sank, J. Wenner, T. C. White, Y. Yin, A. N. Cleland, and J. M. Martinis, Fluctuations from edge defects in superconducting resonators, Appl. Phys. Lett. **103,** 072601 (2013).

[40] A. Romanenko and D. I. Schuster, Understanding quality factor degradation in superconducting niobium cavities at low microwave field amplitudes, Phys. Rev. Lett. **119,** 264801 (2017).

[41] E. D. Black, An introduction to Pound-Drever-Hall laser frequency stabilization, Am. J. Phys. **69,** 79 (2001).

[42] S. E. de Graaf, A. V. Danilov, and S. E. Kubatkin, Accurate real-time monitoring of quality factor and center frequency of superconducting resonators, IEEE Trans. Appl. Supercond. **24,** 1 (2014).

[43] D. Niepce, J. J. Burnett, M. Kudra, J. H. Cole, and J. Bylander, Stability of superconducting resonators: Motional narrowing and the role of Landau-Zener driving of two-level defects, Sci. Adv. **7,** eabh0462 (2021).

[44] J. Burnett, L. Faoro, I. Wisby, V. L. Gurtovoi, A. V. Chernykh, G. M. Mikhailov, V. A. Tulin, R. Shaikhaidarov, V. Antonov, P. J. Meeson, A. Y. Tzalenchuk, and T. Lindström, Evidence for interacting two-level systems from the $1/f$ noise of a superconducting resonator, Nat. Commun. **5,** 4119 (2014).

[45] J. Burnett, T. Lindström, M. Oxborrow, Y. Harada, Y. Sekine, P. Meeson, and A. Y. Tzalenchuk, Slow noise processes in superconducting resonators, Phys. Rev. B **87,** 140501(R) (2013).

[46] S. T. Skacel, C. Kaiser, S. Wuensch, H. Rotzinger, A. Lukashenko, M. Jerger, G. Weiss, M. Siegel, and A. V. Ustinov, Probing the density of states of two-level

tunneling systems in silicon oxide films using superconducting lumped element resonators, Appl. Phys. Lett. **106,** 022603 (2015).

[47] J. D. Brehm, A. Bilmes, G. Weiss, A. V. Ustinov, and J. Lisenfeld, Transmission-line resonators for the study of individual two-level tunneling systems, Appl. Phys. Lett. **111,** 112601 (2017).

[48] S. E. de Graaf, A. Y. Tzalenchuk, and T. Lindström, $1/f$ frequency noise of superconducting resonators in large magnetic fields, Appl. Phys. Lett. **113,** 142601 (2018).

[49] J. Burnett, A. Bengtsson, D. Niepce, and J. Bylander, Noise and loss of superconducting aluminium resonators at single photon energies, J. Phys. Conf. **969,** 012131 (2018).

[50] D. Niepce, J. Burnett, and J. Bylander, High kinetic inductance NbN nanowire superinductors, Phys. Rev. Appl. **11,** 044014 (2019).

[51] https://doi.org/10.5281/zenodo.7728274.